Sensitivity analysis of Na narrowband wind–temperature lidar systems

George C. Papen, William M. Pfenninger, and Dale M. Simonich

The performance and measurement accuracy of Na narrowband wind–temperature lidar systems are characterized. Error budgets are derived that include several effects not previously reported, such as power-dependent spectral characteristics in the frequency reference, magnetic-field-dependent oscillator line strengths (Hanle effect), saturation, and optical pumping. It is shown that the overall system uncertainty is dependent on the power, pulse temporal characteristics, and beam divergence of the laser transmitter. Results indicate that even systems with significant saturation can produce accurate measurements, which implies the prospect of continuous daytime wind and temperature measurements on semidiurnal and diurnal time periods.

1. Introduction

Na narrowband-lidar techniques have been used to measure the fine-scale structure of both temperatures[1–3] and winds[4] near the mesopause region of the atmosphere (~80–105 km). Currently, Na resonance–fluorescence lidars[5] are the only instruments that provide measurements with high spatial and temporal resolution of the wind and temperature structure in this region of the atmosphere, which has historically been one of the most difficult to study experimentally. These data are vital to understanding overall global energy transport and upper-atmospheric chemistry.[6]

Much of the past research has focused on system development as a consequence of the demanding requirements on the laser source. For routine achievement of accurate wind and temperature measurements, the laser transmitter must produce high-energy pulses (tens of millijoules) that are transform limited and have extremely stable spectral characteristics (<1 part in 10^8). The present work expands on the initial error budget for a Na narrowband wind–temperature lidar system[7] and includes other significant error sources not discussed in that previous study. The key aspect of the current analysis is the development of a comprehensive model for the absorption spectrum of Na that includes power-dependent spectral characteristics, magnetic-field-dependent oscillator line strengths (the Hanle effect), saturation, and optical pumping. The model provides estimates of the sensitivity of the wind and temperature measurements to various system parameters, including the power, pulse temporal characteristics, and beam divergence of the laser transmitter.

The paper is organized as follows: Section 2 presents a review of the narrowband-lidar technique. Sections 3 and 4 discuss the physical sources of error and show how the system uncertainty is characterized. Section 5 discusses the results and provides general design considerations for narrowband resonance–fluorescence systems.

2. Na Narrowband-Lidar Technique

Narrowband Doppler lidar techniques with Na resonance fluorescence have been described in several references.[7,8] We extend the previous works by starting with the lidar equation for resonance lidar,[5] which describes the atmospheric response to the probing laser beam:

$$N(z, t) = \frac{C}{z^2}\,\sigma_{\mathrm{eff}}(f, T, v_R, g, I)\rho_{\mathrm{Na}}(z, t) + N_B, \qquad (1)$$

where

$$C = \eta\,\frac{T_a{}^2 P_l \Delta z \Delta t}{(hc/\lambda)}\,\frac{A_R}{4\pi}.$$

G. C. Papen and W. M. Pfenninger are with the Electo-Optic Systems Laboratory (MC-229), University of Illinois at Urbana-Champaign, 1308 West Main Street, Urbana, Illinois 61801. D. M. Simonich is with the Instituto Nacional de Pesquisas Espaciais, C.P. 515, 12201 São José dos Campos, São Paolo, Brazil.

Received 23 December 1993; revised manuscript received 15 August 1994.

0003-6935/95/030480-19$06.00/0.

In Eq. (1), $N(z, t)$ is the total number of photons detected (photocounts) from the volume element, with thickness Δz that is centered at altitude z, summed over the time interval t to $t + \Delta t$. The average Na density is $\rho_{Na}(z, t)$, and the total background noise in the signal in this time interval is N_B. C is a constant that depends on the one-way atmospheric transmittance T_a and the average power of the laser P_l, with photon energy hc/λ, where h is Plank's constant, c is the speed of light, and λ is the laser wavelength. Backscattered photons are detected by a telescope with area A_R and efficiency η. Because the concentration of absorbing atoms is low in the mesopause, the effects of extinction are ignored.

The effective-backscatter cross section, $\sigma_{eff}(f, T, v_R, g, I)$ in Eq. (1), provides all the information about the photon–atom scattering process. In resonance fluorescence it is the integrated product of the atmospheric-Na cross section $\sigma_{Na}(f', T, v_R, I)$ and the line shape of the laser pulse $g(f' - f_l)$ with center frequency f_l:

$$\sigma_{eff}(f_l, T, v_R, g, I) = \int_{-\infty}^{\infty} g(f' - f_l)\sigma_{Na}(f', T, v_R, I)\mathrm{d}f', \quad (2)$$

where T is the temperature, v_R is the wind velocity, and I is the laser intensity.

The dependence of σ_{Na}, and thus σ_{eff}, on T and v_R provides the fundamental physical reference used in the narrowband-lidar technique. Measurements of σ_{eff} at three different laser frequencies are necessary to determine $\rho_{Na}(z, t)$, T, and v_R completely. However, because σ_{eff} also depends on the spectral and temporal characteristics of the laser pulse, the lidar system must be carefully designed to minimize errors that are introduced by these sources. The goal of this work is to characterize accurately the dependence of σ_{eff} on each narrowband-lidar system parameter and to show how errors in these parameters affect temperature and wind measurements.

The University of Illinois wind/temperature lidar (W/TL) measures σ_{eff} at four different frequencies to permit nearly independent determinations of T and v_R. For each measurement, the narrow-bandwidth laser is tuned to excite only a small portion of the Na absorption spectrum. Backscattered fluorescence is collected through a telescope with a bandwidth large enough to detect the entire Na spectrum. From the time delay between the laser pulse and the fluorescence signal, a range-resolved profile of the backscatter is generated. Summation of this range-resolved signal over multiple laser pulses increases the signal-to-noise ratio, which generates a vertical profile of the average Na-fluorescence response. Profiles are grouped in pairs by the laser tuning frequency, as determined by the parameter to be extracted (T or v_R). The background noise N_B term is then subtracted from each profile, and the ratio for each pair is formed by

$$R(z, t, \tau) = \frac{N_{f_1}(z, t + \tau)}{N_{f_2}(z, t)} = \frac{\sigma_{eff}(f_1, T, v_R, g, I)\rho_s(z, t + \tau)}{\sigma_{eff}(f_2, T, v_R, g, I)\rho_s(z, t)}, \quad (3)$$

where $N_{f_1}(z, t + \tau)$ and $N_{f_2}(z, t)$ are the signal counts at frequencies f_1 and f_2 that were recorded at times t and $t + \tau$. Because of the finite laser-tuning time, the interval between successive measurements τ will always be greater than the integration time at each frequency Δt. If the time between measurements is small relative to perturbations in the Na density $[\rho_a(t) \approx \rho_a(t + \tau)]$ and if the response is linear $[\sigma_{eff}(f_1, T, v_R, g, I) \approx \sigma_{eff}(f_1, T, v_R, g)]$, Eq. (3) becomes

$$R = \frac{N_{f_1}(z, t + \tau)}{N_{f_2}(z, t)} \approx \frac{\sigma_{eff}(f_1, T, v_R, g)}{\sigma_{eff}(f_2, T, v_R, g)}. \quad (4)$$

Equation (4) is the starting point for most analyses of Na narrowband lidars because it is no longer necessary to know the absolute value of any parameter, just it's relative contribution.

Of the mesospheric metals, Na is preferred because of its high concentration, large backscatter coefficient, and relatively long chemical lifetime.[9] In addition, the spectroscopy of the Na D_2 lines is well known, with the locations of the underlying hyperfine lines known to within 500 kHz[10] (an overview of Na spectroscopy is given in Appendix A). Because Zeeman splitting of the hyperfine states of Na (which is due to the geomagnetic field) is small compared with the linewidth of the laser pulse, we may approximate the true Na cross section by a sum of six Doppler-broadened transitions, each is weighted by the strength of the corresponding hyperfine transition:

$$\hat{\sigma}_{Na}(f', T, v_R) = \frac{1}{(2\pi\sigma_D^2)^{1/2}} \sum_i A_i \times \exp\left[\frac{-(f' - f_i + v_R/\lambda)^2}{2\sigma_D^2}\right], \quad (5)$$

where f_i is the center frequency of the hyperfine transition with strength A_i. The Doppler-broadened linewidth is $\sigma_D^2 = k_B T/m_{Na}\lambda^2$, where k_B is Boltzmann's constant and m_{Na} is the mass of a Na atom. The term v_R/λ is the Doppler shift associated with the radial-wind velocity. The cross section $\hat{\sigma}_{Na}(f', T, v_R)$ given by Eq. (5) provides the physical reference for both temperature and wind measurements and is plotted as a function of T and v_R in Figs. 1 and 2.

An analytic expression for the effective-backscatter cross section may be obtained if the laser line shape $g(f)$ is approximated by a Gaussian with rms line-

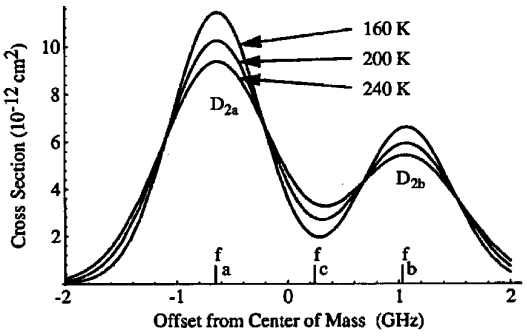

Fig. 1. Linear absorption backscatter cross section of the Na D_2 line as a function of frequency for several temperatures. As the temperature increases, the ratio $(R_T = N_{f_c}/N_{fa})$ of the backscatter from two frequencies f_c and f_a increases and thereby provides a discriminant for the determination of the temperature.

width σ_{rms}:

$$\hat{g}(f) = \frac{1}{(2\pi\sigma_{\mathrm{rms}}{}^2)^{1/2}} \exp\left[-\frac{f^2}{2\sigma_{\mathrm{rms}}{}^2}\right]. \tag{6}$$

The integration of Eq. (2) is now analytic and yields an approximate form $\hat{\sigma}_{\mathrm{eff}}$ for σ_{eff} that depends only on σ_{rms} and not on the detailed line shape $g(f)$:

$$\hat{\sigma}_{\mathrm{eff}}(f_l, T, v_R, \sigma_{\mathrm{rms}}) = \frac{1}{(2\pi\sigma_e{}^2)^{1/2}} \sum_i A_i \times \exp\left[-\frac{(f_l - f_i + v_R/\lambda)^2}{2\sigma_e{}^2}\right], \tag{7}$$

where $\sigma_e{}^2 = \sigma_{\mathrm{rms}}{}^2 + \sigma_D{}^2$. Although the measured line shape is not exactly Gaussian, Eq. (7) provides an excellent approximation when $\sigma_{\mathrm{rms}} \ll \sigma_D$ that is suitable for the analytical determination of the relative error contributions (see Section 3).

Once the functional form of $\hat{\sigma}_{\mathrm{eff}}$ is known, the optimal frequency operating point Q for f_1 and f_2 depends on the type of measurement. For accurate temperatures, f_1 and f_2 are chosen such that R_T is a sensitive function of T at the temperature operating point Q_T, i.e., $\partial R_T/\partial T|_{Q_T}$ is large, and is insensitive to radial winds, i.e., $\partial R_T/\partial v_R|_{Q_T}$ is small. An examination of Fig. 1 shows that the optimal choice for Q_T is frequencies at the maximum and local minimum of σ_{Na}, where the temperature dependence of R_T is largest. At each of these two points, the cross section is relatively insensitive to radial-wind fluctuations. We denote these frequencies by f_a near the peak of the D_{2a} resonance and f_c near the midpoint between the D_{2a} and D_{2b} resonances. As the Na temperature increases, σ_{Na} broadens and the ratio of the backscatter coefficients $R_T = N_{f_c}/N_{f_a}$ increases. These frequencies are near optimal and are chosen because absolute frequency markers with large discriminants can be generated at these locations through the use of Doppler-free spectroscopy (see Appendix A).

Radial-wind velocities are determined by the measurement of the Doppler shift of the Na atoms along the beam path. A positive wind component towards the laser, v_R, shifts the absorption spectrum of the atmospheric Na by $-v_R/\lambda$, where λ is the laser wavelength. The minus sign arises because, for a fixed laser frequency and $v_R > 0$, photons from the laser interact with an absorption spectrum that is *downshifted* in frequency with respect to the zero-wind spectrum. The maximum variation in R_W occurs for measurements taken on each side of the D_{2a} resonance, at f_+ and f_-. As the velocity increases toward the laser $(v_R > 0)$, the ratio of returns $R_{W_1} = N_{f_+}/N_{f_-}$ decreases. Conveniently, the cross section in these regions is also relatively insensitive to temperature variations. Ignoring the contribution of the D_{2b} feature and using the analytic expression for the absorption cross section [Eq. (7)], we find that the optimal frequencies are $f_\pm = f_a \pm \sqrt{2}\sigma_D$.[7] The actual frequencies used for the W/TL system are $f_\pm = f_a \pm$ 600 MHz. These were chosen because they can be generated with a commercial Fabry–Perot interferometer.

As previously mentioned, measurement of the cross section at only three frequencies $(f_a, f_+,$ and $f_c)$ is sufficient to determine both the radial-wind velocity and the temperature. For a system based on this three-frequency technique (W_2), the wind ratio is $R_{W_2} = N_{f_+}/N_{f_a}$. W_2 is more sensitive to temperature errors than the first wind measurement (W_1) technique (i.e., $\partial R_{W_2}/\partial T|_{Q_{W_2}} > \partial R_{W_1}/\partial T\,|_{Q_{W_1}}$, where Q_{W_1} and Q_{W_2} are the operating points), but W_2 is being investigated because fewer measurements are required for each wind–temperature sequence and because frequency tuning may be done on a shot-to-shot basis with an acousto-optic cell,[11] which reduces the errors caused by density fluctuations.

Although the frequencies for the measurements have been determined with an approximate line shape, the ratio R in Eq. (4) that is used in data analysis is

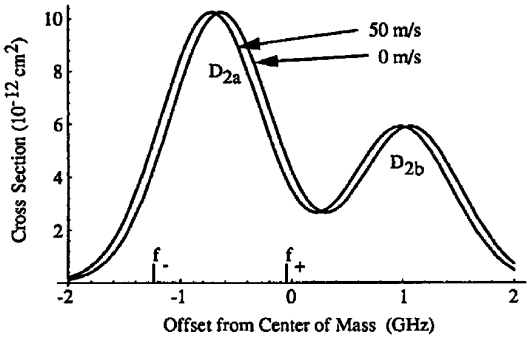

Fig. 2. Absorption backscatter cross section of the Na D_2 line as a function of frequency for two radial-wind velocities. For radial-wind velocities toward the receiver, the ratio of the backscatter from two frequencies f_+ and f_- that are shown in the figure decreases.

calculated with the measured line shape $g(f)$ and becomes a function of only T and v_R. A look-up table, which is generated with $R(T, v_R)$, provides the inverse functions $T(R_T, v_R)$ and $v_R(R_W, T)$. Because these inverse functions are coupled, an initial guess v_{R_0} is made for v_R, and the temperature is calculated from $T(R_T, v_R = v_{R_0})$. This temperature T_0 is then used to determine v_R, from the other look-up table, $v_R(R_W, T = T_0)$. Multiple iterations may have to be performed until v_R and T converge.

3. Determination of σ_{Na}

Accurate measurements with the narrowband technique require exact knowledge of the Na-backscatter cross section. In general, σ_{Na} must be determined from the solution to the density matrix that includes all 24 Zeeman states. However, we may use the approximate cross section of Eq. (5) if we carefully choose the strengths of the six transitions. In this section, we discuss two physical mechanisms: the Hanle effect and saturation. They determine the coefficients A_i in Eq. (5). Their contribution to the overall measurement uncertainty will be discussed in Section 4.

A. Hanle Effect

When an atom is placed in a magnetic field, **B**, it is convenient to represent all electronic wave functions with respect to an axis along the magnetic field. Atoms then absorb radiation in one of three polarizations defined with respect to **B**. A π photon (which indicates linear polarization along the magnetic field) excites transitions between Zeeman substrates with the same magnetic quantum number m (see Appendix A for a description of the Na eigenstates), while a $\sigma^{\pm}$ photon (circularly polarized perpendicular to **B**, where the minus sign denotes right-circular polarization and the plus sign denotes left circular polarization) excites transitions in which $\Delta m = \pm 1$. Thus the π and $\sigma^{\pm}$ polarizations form a basis set to describe the polarization of the absorbed and the emitted radiation.

During the resonance–fluorescence process, the magnetic field interacts with occupied atomic states to change their states of polarization. This interaction takes place by means of a $\mathbf{v} \times \mathbf{B}$ term (where **v** is the velocity of the electron) and causes a precession of the harmonic oscillator and a change of polarization of each Zeeman–substate transition.[12] This results in a change in the emitted-radiation pattern from its zero-magnetic-field value. Because we are interested only in backscattered radiation, these changes in radiation patterns can be represented as changes in the relative oscillator strengths of the six hyperfine lines, for which we define each A_i as a sum over the corresponding Zeeman transitions. In the mesopause region above the Urbana Atmospheric Observatory (UAO), the declination of the Earth's magnetic field is nearly zero and the inclination is 70° (declination is defined as the clockwise angle between geographic north and the projection of the magnetic field onto the horizontal plane; inclination is defined as the downward angle between the projection of the magnetic field onto the horizontal plane and the magnetic field). Computations discussed in Appendix A yield the relative oscillator-strength ratios for the case of vertical transmission and reception at UAO as 5:5.49:2:15.64:5:0.98 as opposed to 5:5.5:2:15.68:5:0.98 for the zero-magnetic-field case. Ignoring the Hanle effect through the use of the spatially averaged oscillator strengths (5:5:2:14:5:1) in data analysis introduces a temperature bias of 1.4 K and a radial-wind-velocity bias of 0.7 m/s.

B. Saturation and Optical Pumping

For large pulse intensities, the intensity dependence of σ_{Na} becomes important because single atoms no longer respond in the linear fashion that is assumed for the calculation of the transition strengths described above. Saturation and optical-pumping effects must be included to determine the true A_i for use in Eq. (5).

In the low-intensity limit, the laser pulse excites one of the six hyperfine transitions and causes electrons from one of the ground states to populate the corresponding upper state. The upper state then decays back to one of the ground states in an average period that is determined by the upper-state lifetime. Saturation occurs when another photon causes stimulated emission of the electron in the upper state and thus removes the stimulated photon from natural decay, which effectively reduces the upper-state lifetime. This stimulated emission occurs along the outgoing beam and decreases the backscatter cross section. In addition, occupation of an upper state decreases further absorption into that state and results in a reduced effective-backscatter cross section. As the laser intensity increases, these two effects can cause a systematic measurement error, because each of the six transitions that compose the Doppler-broadened line shape saturates at a different intensity. In addition, saturation is more pronounced for narrow-linewidth pulses because the energy of the laser is distributed over fewer transitions.

Finally, if the linewidth of the outgoing pulse (~125 MHz FWHM for the W/TL system) is smaller than the separation of the two ground-state manifolds (~1.8 GHz), the pulse can induce transitions from each individual ground state. Optical pumping occurs when the excited atoms relax to the opposite ground state (see Appendix A). As direct equalization between the two ground states in the atmosphere is negligible,[12] optical pumping reduces the density of atoms available to absorb the incoming laser radiation, which reduces the effective-backscatter cross section. For example, when the pulse is tuned to the D_{2a} peak, atoms excited from the $f = 1$ state can relax back to the $f = 2$ state (see Fig. 7 in Appendix A). Once in the $f = 2$ state, atoms cannot return to the $f = 1$ state (the direct transition is negligible on the time scale of the interaction and the pulse is spectrally too narrow for excitation back out of the $f = 2$ state).

Therefore, these atoms are removed from further absorption. In the limit in which almost all the atoms exist in the $f = 2$ state, the $f = 1$ state is completely bleached and no further absorption can occur from the $f = 1$ ground state. Laser pulse lengths that are shorter than the lifetimes of the excited states do not suffer from optical-pumping effects because no significant shift in the ground-state population can occur. As the laser pulse length increases, the error induced by optical pumping becomes more significant.

Saturation effects have been considered by several groups.[13,14] A rate-equation simulation of atomic Na is discussed in Appendix B; it uses a realistic temporal pulse envelope and a Gaussian transverse spatial distribution to compare the true Na response with an extrapolation of the low-intensity, linear response. To simplify computations, one may replace the actual temporal and spatial functions with rms quantities,[13] although this method was not employed in this analysis.

Figures 3 and 4 show the general trends for saturation- and pumping-induced errors as functions of the outgoing beam characteristics. Figure 3(a) shows the percent saturation at the backscatter peak f_a as a function of the pulse energy for a fixed pulse duration of 7 ns (rms). Figure 3(b) shows the effects of a change in the pulse duration for a fixed energy (100 mJ/pulse). Note that a 100-mJ pulse that produces 5% saturation if the pulse is 7 ns long will only produce 0.5% saturation if the pulse length is 100 ns long, which emphasizes the importance of the use of low peak power systems. However, saturation cannot be reduced to zero with an increasing pulse length because of the increased importance of optical pumping. Minimum saturation is approximately 0.3% for 100-mJ pulses with a duration greater than 600 ns.

Figure 4(a) plots the percent saturation for a 7-ns (rms) pulse at both f_a and f_c for two pulse energies (35 mJ and 100 mJ) as a function of the outgoing beam divergence. The relative errors at f_a and f_c increase concurrently, which indicates that the ratio R_T may be relatively insensitive to saturation. To confirm this, Figs. 4(b) and 4(c) show the effect of saturation on the relative error in the ratio $\Delta R/R$ and on the absolute error for the same parameters used in Fig. 3. On the left-side vertical axis in Figs. 4(b) and 4(c) is $\Delta R/R$, the relative error from saturation. On the right-side vertical axis is the absolute error if we derive temperatures and wind velocities using the low-intensity cross section (the calculation of absolute error is discussed in the next section). It is important to remember that, although individual profiles can have large relative errors that are due to saturation effects [as shown in Fig. 4(a)], the overall relative error in the ratio and the absolute error [Figs. 4(b) and 4(c)] are significantly diminished because

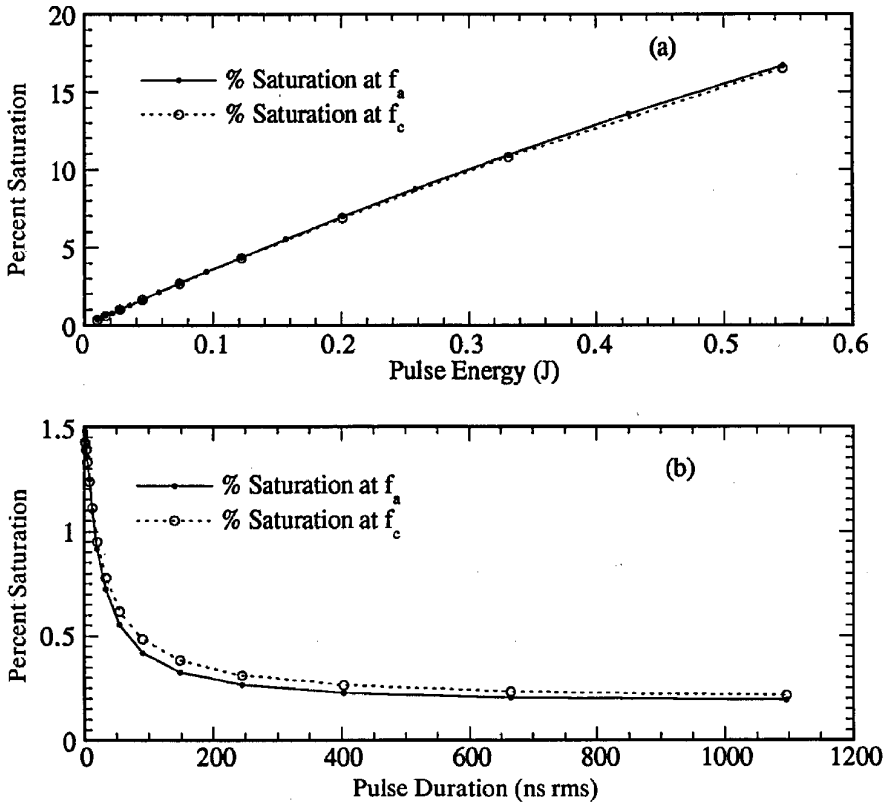

Fig. 3. (a) Deviation from linear response (percent saturation) as a function of the total pulse energy for a 1-mrad, 7-ns rms pulse. Details of the calculation are presented in Appendix B. The calculated points are represented by the filled and open circles. The curves are drawn to aid the viewer. (b) The same as in (a) except that the pulse energy is held at a constant 100 mJ and the independent variable is the pulse duration. The limit of the response at ~0.3% for pulses longer than 600 ns is caused by optical-pumping effects.

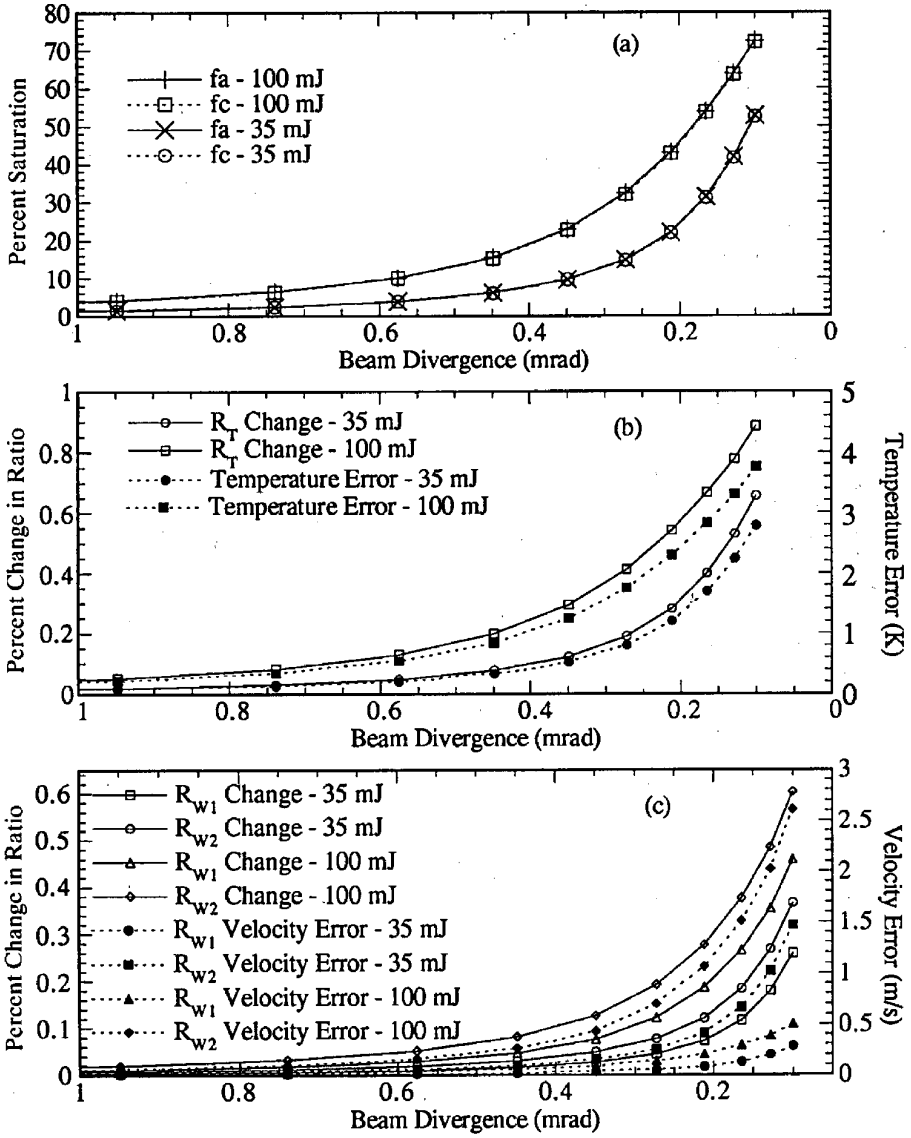

Fig. 4. (a) Percent saturation as a function of divergence at f_a and f_c for two pulse energies (35 mJ and 100 mJ) for a 7-ns rms pulse. (b) Temperature error for the same parameters as given for Fig. 3. The y axis on the left-hand side of the figure shows the relative error in the ratio $\Delta R_T/R_T$. The right-hand-side y axis shows the temperature error determined with the values in Table 2. (c) Wind-velocity error for both wind-measurement techniques (W_1 and W_2) for the same parameters given for Fig. 3.

both terms in the ratio have approximately the same functional dependence on the intensity.

4. System Characterization

Whereas the previous section discussed errors that are due to imprecise calibration of σ_{Na}, this section presents the properties of the measurement process that reduce the accuracy of derived temperatures and wind velocities. These errors can result in both systematic errors (which are due to incorrect absolute frequency calibration or incorrect laser line shape) and random errors (which are due to laser frequency jitter, shot noise, and atmospheric-density fluctuations). These system errors are then converted to temperature and wind errors by the use of differentials of the corresponding ratio. Although the analysis quotes specific numbers for the W/TL system, the procedures are general and can be applied to a variety of resonance–fluorescence systems.

A. Systematic Error

1. Absolute Frequency Calibration

Accurate knowledge of the absolute laser frequency is essential to both temperature and wind-velocity measurements. For example, a frequency-calibration offset of 5 MHz will introduce a 0.5-K error in derived temperatures and a 3-m/s error in derived wind velocities for the W/TL system. Of all the independent system parameters, the error associated with the absolute frequency of the outgoing beam is the hardest to ascertain. The absolute frequency reference in the W/TL system uses the Doppler-free features of a Na-vapor cell to control the frequency of

a cw ring dye laser. Because the pulsed dye amplifier that generates the outgoing pulse is seeded by the dye laser, the frequency accuracy of the vapor-cell response is transferred to the pulse.

With nonlinear Doppler-free spectroscopy, the doublet nature of Na provides two convenient frequency markers at f_a and f_c with frequency discriminants much greater than those obtainable with linear absorption spectroscopy (see Appendix B). For accurate measurements, these markers must be referenced to the *linear* backscatter cross section σ_{Na}, which is measured in the atmosphere.

The Doppler-free cross section of Na differs considerably from its linear counterpart for several reasons. First, Doppler broadening is greater in the vapor cell because the Na-vapor density and temperature are considerably larger than in the atmosphere. Second, the D_{2a} and D_{2b} resonances show Lamb dips owing to saturation effects, and a resonance enhancement (called the crossover) occurs midway between the D_{2a} and D_{2b} lines as a result of concurrent excitation from both ground states. Because the Lamb dips and crossover are caused by nonlinear effects, they change shape as the laser intensity varies. These intensity-dependent spectral features of the vapor cell can be a significant source of frequency error.

To assess the error associated with improper absolute frequency calibration, a rate-equation simulation of the nonlinear vapor-cell response that incorporates the six hyperfine states is used to model the Doppler-free frequency response from which absolute frequencies can be determined. A full description of the simulation is provided in Appendix B. Correlation between measured and simulated Doppler-free responses provides an absolute frequency-calibration estimate within ± 2 MHz. It is shown in Subsection 4.C that the laser's frequency-calibration error does not dominate the total system error.

2. Line-shape Measurement

The outgoing laser line shape $g(f)$ influences the derived temperature and wind velocities because the effective-backscatter cross section σ_{eff} is the integrated product of the Na cross section σ_{Na} and the line shape $g(f)$. Therefore, discrepancies between the line shape used in data reduction and the true line shape introduce temperature and wind-velocity errors. In addition, as the spectral width of $g(f)$ increases, the sensitivity of the technique $(\partial R_T/\partial T|_{Q_T})$ decreases from convolutional averaging; this result stresses the importance of the use of narrow-bandwidth pulses for the transmitter.

The line shape of the outgoing laser pulse is determined by measurement of the spectral content of the pulse with a narrowband étalon (with a free spectral range of 2 GHz and a finesse of 200) and a boxcar integrator. As the étalon is scanned through the pulse line shape, the boxcar provides samples of the pulse spectral content that are integrated over multiple laser shots. After deconvolving the transmission characteristics of the étalon (10 MHz FWHM), the measured line shape $g(f)$ is used to calculate σ_{eff}, and the lookup tables for the inverse functions $T(R_T, \nu_R)$ and $\nu_R(R_W, T)$ are generated. For error analysis, $g(f)$ is fitted by a Gaussian with rms width, σ_{rms}. This fitted rms width ($\sim$60 MHz for the W/TL system) is then used in Eq. (7) to determine $\hat{\sigma}_{eff}$.

It has been noted that the pulse line shape must be measured on a regular basis because the outgoing spectral characteristics can change significantly with laser alignment.[7] The rms linewidth uncertainty, which is caused by routine realignment of the amplifier between line-shape measurements, is estimated to be ± 4 MHz.

B. Random Error

1. Jitter

The random uncertainty associated with laser and electronic jitter will vary from system to system. To quantify the laser and electronic jitter for the current system, tuning feedback data are accumulated from the vapor cell and the Fabry–Perot interferometer that produces $f_{\pm}$ for the wind measurements. After they have been converted to frequencies with the calibrated vapor-cell and interferometer responses, the mean and variance of these data determine laser jitter for each profile and over the entire night. Figure 5 shows a typical trace for the stability of the peak frequency f_a for the W/TL system over the night of 17 January 1993 at UAO (other nights are similar). Table 1 shows the standard deviation σ_j for each tuning location taken from the data. Over the whole night, the standard deviation is less than 2.2 MHz for each tuning location.

2. Density Fluctuations

One of the key assumptions to the use of Eq. (4) for the determination of R is that the density variations over a measurement interval are small $[\rho_s(t) \approx \rho_s(t + \tau)]$. In practice, density variations introduce errors into the temperature and wind measurements because the apparent backscatter coefficient changes between profiles. The resulting relative error is a function of the integration time Δt and the distance z from the centroid of the Na layer and may

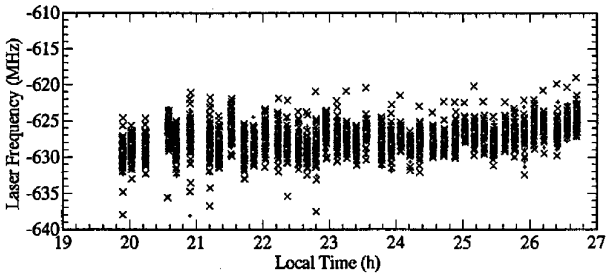

Fig. 5. Measurement of the jitter at f_a for the night of 17 January 1993 at the UAO in Urbana, Illinois.

Table 1. rms Jitter Measurements at f_a for the University of Illinois Wind-Temperature Lidar for the Night of 17 January 1993

Location	f (MHz)	σ_j (MHz)
f_-	−1238	1.22
f_a	−638	1.48
f_+	−38	1.45
f_c	232	1.41

be written as[15]

$$\frac{\Delta R(z,\tau)}{R} \approx \frac{1}{T_{\rm rms}}\frac{(2\pi\Delta t)}{(\gamma-1)}\left[1-(z-z_0)\gamma H/\sigma_0^2\right]\langle(r_a^2)\rangle^{1/2}, \tag{8}$$

where σ_0 is the rms thickness of the unperturbed Na layer ($\sim$4.2 km), H is the atmospheric scale height ($\sim$6 km), z_0 is the layer centroid height ($\sim$92 km), γ is the ratio of specific heats (1.4), $T_{\rm rms}$ is the wave-field correlation time, and $\langle r_a^2\rangle$ is the variance of the relative atmospheric perturbations. We note that weighted averaging can significantly reduce the density fluctuations given by Eq. (8).[16] We present both the derivation of Eq. (8) and the forms for reducing the error by averaging in Appendix C.

3. Shot Noise

Shot noise ultimately limits the measurement accuracy of any photon-counting system because no amount of system design can remove the statistical nature of the photon-detection processes. The physics of the photon-counting process are well known, and for the ratio-calculation technique that we used, $\Delta R_T/R_T$, the change in the ratio as a function of the number of photons at the peak N_{f_a} is given by[7]

$$\frac{\Delta R_T}{R_T} \approx \frac{1}{(N_{f_a})^{1/2}}\left(1+\frac{1}{R_T}\right)^{1/2} \tag{9a}$$

where $R_T \approx 0.28$ at the operating point Q_T.

Through a similar technique, the shot-noise error for the two wind measurements can also be expressed in terms of N_{f_a}:

$$\frac{\Delta R_{W_1}}{R_{W_1}} \approx \frac{1}{(N_{f_+})^{1/2}}\left(1+\frac{1}{R_{W_1}}\right)^{1/2} = \frac{1}{(N_{f_a})^{1/2}}\left(\frac{R_{W_1}}{R_{W_2}}+\frac{1}{R_{W_2}}\right)^{1/2} \approx \frac{1}{(N_{f_a})^{1/2}}\left(\frac{2}{R_{W_2}}\right)^{1/2}, \tag{9b}$$

$$\frac{\Delta R_{W_2}}{R_{W_2}} \approx \frac{1}{(N_{f_a})^{1/2}}\left(1+\frac{1}{R_{W_2}}\right)^{1/2}, \tag{9c}$$

where $R_{W_1} \approx 1$ is used in Eq. (9b) to facilitate comparison of the techniques.

C. Error Calculations

Through the use of differentials of the ratios and Eq. (7), uncertainties in system parameters can be converted into uncertainties in derived temperatures and radial-wind velocities.

The backscatter ratio used to derive temperature errors is

$$\hat{R}_T(f_a, f_c, T, v_R, \sigma_{\rm rms}) = \frac{\hat{\sigma}_{\rm eff}(f_c, T, v_R, \sigma_{\rm rms})}{\hat{\sigma}_{\rm eff}(f_a, T, v_R, \sigma_{\rm rms})}, \tag{10}$$

and the two ratios for wind-velocity errors are

$$\hat{R}_{W_1}(f_-, f_+, T, v_R, \sigma_{\rm rms}) = \frac{\hat{\sigma}_{\rm eff}(f_+, T, v_R, \sigma_{\rm rms})}{\hat{\sigma}_{\rm eff}(f_-, T, v_R, \sigma_{\rm rms})}, \tag{11}$$

$$\hat{R}_{W_2}(f_a, f_+, T, v_R, \sigma_{\rm rms}) = \frac{\hat{\sigma}_{\rm eff}(f_+, T, v_R, \sigma_{\rm rms})}{\hat{\sigma}_{\rm eff}(f_a, T, v_R, \sigma_{\rm rms})}. \tag{12}$$

The derivatives of each of these ratios with respect to each of the system parameters are

$$\frac{\partial\hat{R}}{\partial\chi} = \hat{R}\left[\frac{\hat{\sigma}_{\rm eff}'(f_1)}{\hat{\sigma}_{\rm eff}(f_1)} - \frac{\hat{\sigma}_{\rm eff}'(f_2)}{\hat{\sigma}_{\rm eff}(f_2)}\right], \tag{13}$$

where the prime denotes the derivative with respect to χ and χ is one of the following: $\{f_1, f_2, T, v_R, \sigma_{\rm rms}\}$. Note that to determine analytic expressions for these ratios, we have used the approximate expression for the effective-backscatter cross section, $\hat{\sigma}_{\rm eff}$.

By evaluation of the differential at the operating point, errors that are introduced by shot noise, density variations, and saturation can be calculated. For example, the temperature error ΔT that is associated with an error in the ratio ΔR is given by

$$\Delta T = \Delta R_T \frac{\partial T}{\partial\hat{R}_T}\bigg|_{Q_T} = \frac{\Delta R_T}{\hat{R}_T}\left[\frac{\hat{\sigma}_{\rm eff}'(f_c)}{\hat{\sigma}_{\rm eff}(f_c)} - \frac{\hat{\sigma}_{\rm eff}'(f_a)}{\hat{\sigma}_{\rm eff}(f_a)}\right]^{-1}\bigg|_{Q_T}. \tag{14}$$

Similar expressions can be derived for wind-velocity errors.

Uncertainties that are due to other system parameters can be calculated by ratios of partial derivatives at Q. For example, the variation in derived temperature ΔT with respect to a change in the wind velocity Δv_R is

$$\Delta T = \frac{\partial\hat{R}_T}{\partial v_R}\Big/\frac{\partial\hat{R}_T}{\partial T}\bigg|_{Q_T}\Delta v_R, \tag{15}$$

and the variation in derived wind velocity Δv_R with respect to a change in the temperature ΔT is

$$\Delta v_R = \frac{\partial\hat{R}_W}{\partial T}\Big/\frac{\partial\hat{R}_W}{\partial v_R}\bigg|_{Q_W}\Delta T. \tag{16}$$

The derivatives and their magnitudes have been evaluated for an operating point Q (T = 200 K, v_R = 0 m/s, f_a = −638 MHz, f_c = 232 MHz, f_- = −1238 MHz, f_+ = 38 MHz, and $\sigma_{\rm rms}$ = 60 MHz) and are

Table 2. Ratio R[a] Calculated with Eqs. (7) and (10)–(12), Measurement Errors, and Derivatives[b] Calculated with Eq. (13) for Wind and Temperature Differentials

	Temperature Differentials	Wind Differentials	
		W_1	W_2
Ratio R	$R_T = 0.281$	$R_{W_1} = 1.07$	$R_{W_2} = 0.460$
Calculated with	N_{f_c}/N_{f_a}	N_{f_+}/N_{f_-}	N_{f_+}/N_{f_a}
Error	$\Delta T = 118\,\dfrac{\Delta R_T}{R_T}$	$\Delta v_R = 116\,\dfrac{\Delta R_{W_1}}{R_{W_1}}$	$\Delta v_R = 262\,\dfrac{\Delta R_{W_2}}{R_{W_2}}$
Derivatives	$\dfrac{\partial T}{\partial f_a} = 0.0002\,\dfrac{\text{K}}{\text{MHz}}$	$\dfrac{\partial v_R}{\partial f_-} = 0.327\,\dfrac{\text{m/s}}{\text{MHz}}$	$\dfrac{\partial v_R}{\partial f_a} = 0.0004\,\dfrac{\text{m/s}}{\text{MHz}}$
	$\dfrac{\partial T}{\partial f_c} = 0.102\,\dfrac{\text{K}}{\text{MHz}}$	$\dfrac{\partial v_R}{\partial f_+} = 0.262\,\dfrac{\text{m/s}}{\text{MHz}}$	$\dfrac{\partial v_R}{\partial f_+} = 0.570\,\dfrac{\text{m/s}}{\text{MHz}}$
	$\dfrac{\partial T}{\partial \sigma_{\text{rms}}} = 0.115\,\dfrac{\text{K}}{\text{MHz}}$	$\dfrac{\partial v_R}{\partial \sigma_{\text{rms}}} = 0.0101\,\dfrac{\text{m/s}}{\text{MHz}}$	$\dfrac{\partial v_R}{\partial \sigma_{\text{rms}}} = 0.146\,\dfrac{\text{m/s}}{\text{MHz}}$
	$\dfrac{\partial T}{\partial v_R} = 0.174\,\dfrac{\text{K}}{\text{m/s}}$	$\dfrac{\partial v_R}{\partial T} = 0.0874\,\dfrac{\text{m/s}}{\text{K}}$	$\dfrac{\partial v_R}{\partial T} = 1.27\,\dfrac{\text{m/s}}{\text{K}}$

[a] For an operating point Q with $T = 200$ K, $v_R = 0$ m/s, $f_a = -638$ MHz, $f_c = 232$ MHz, $f_- = -1238$ MHz, $f_+ = 38$ MHz, and $\sigma_{\text{rms}} = 60$ MHz.
[b] Magnitudes of derivatives with respect to the other system parameters.

summarized in Table 2. Note that these derivatives depend on the operating point and thus must be recalculated for each system. For example, a 20% increase in these values will yield an ~40% increase in the estimated number of photons required (from shot-noise error calculations) to maintain the same signal-to-noise ratio.

Table 3 shows the effect of frequency, linewidth, density variation, and saturation on temperature and wind measurements for the W/TL operating point. From Tables 2 and 3, temperature and wind errors are plotted as a function of beam divergence on the right-hand-side y axis of Figs. 4(b) and 4(c).

If all error sources are independent, the total

Table 3. Magnitude of Wind- and Temperature-Measurement Errors for Each System Parameter and Measurement Technique[a]

System Parameter	Source Uncertainty		Temperature Uncertainty (K)	Wind-Velocity Uncertainty	
	Temperature	Wind		W_1 (m/s)	W_2 (m/s)
Frequency[b]					
Δf_-	2.36 MHz	2.36 MHz		0.77	
Δf_a	2.49 MHz	2.49 MHz	0.0002		0.0004
Δf_+	2.47 MHz	2.47 MHz		0.65	1.45
Δf_c	2.45 MHz	2.45 MHz	0.26		
Lindwidth					
$\Delta \sigma_{\text{rms}}$	4 MHz	4 MHz	0.46	0.04	0.58
Density (at altitude)[c]					
84 km	0.122%	0.122%	0.14	0.14	—
92 km	0.025%	0.025%	0.03	0.03	—
100 km	0.07%	0.07%	0.08	0.08	—
Saturation					
35 mJ pulse and beam divergence of					
1.0 mrad	0.02%	0.005%	0.024	0.005	0.013
0.5 mrad	0.08%	0.02%	0.095	0.023	0.052
0.1 mrad	0.7%	0.37%	0.83	0.43	0.97
100 mJ pulse and beam divergence of					
1.0 mrad	0.6%	0.01%	0.071	0.012	0.026
0.5 mrad	0.19%	0.06%	0.23	0.070	0.16
0.1 mrad	0.9%	0.56%	1.1	0.65	1.5
Wind error for temperature		1 m/s	0.017		
Temp error for wind	1 K			0.087	1.27

[a] Blank entries occur because only two frequencies are used to determine each system's measurement.
[b] Calculated with $\Delta f = (\sigma_j^2 + \sigma_c^2)^{1/2}$ σ_j jitter error (see Table 1) and a σ_c calibation error of 2 MHz.
[c] Calculated for $\Delta t = 60$ s with weighted averaging through the use of $\omega_c = 5$ min for columns 1 and 2 (see Appendix C for details) and $\Delta t \sim 1$ s, causing negligible error, for column 3.

system uncertainty without shot noise σ_{total} is the rms sum of all the individual uncertainty sources σ_i.

$$\sigma_{\text{total}} = \left(\sum_i \sigma_i^2 \right)^{1/2}, \tag{17}$$

where σ_i^2 are the variances of the individual error sources. The results for the W/TL system are summarized in Table 4. Using Eqs. (9a)–(9c), we can then determine the total number of photons N_{f_a} that must be detected at frequency f_a such that the shot-noise error is no larger than the rest of the system error. These values are also given in Table 4. For temperature measurements, the large signal required for the shot-noise uncertainty to be comparable to the rest of the system uncertainty indicates that the current system is shot-noise limited for temperatures and nearly shot-noise limited for winds.

5. Discussion

The most remarkable feature illustrated by the data in Table 3 is the insensitivity of the temperature and wind measurements to saturation effects. Although each of the individual lines can have significant saturation [shown in Fig. 4(a)], the overall error that is due to saturation is smaller than one might expect. This relative insensitivity has one very important implication: Present systems are limited to nighttime operation because of large daytime background counts. To reduce the daytime noise counts, beam expanders are typically used to reduce the divergence of the outgoing beam, which allows the receiver to use a smaller field of view and thus reduces the background counts. However, decreasing the divergence increases the beam intensity at the Na layer, and, to date, daytime measurements have not been attempted because of concerns about saturation. Examination of Fig. (4) and Table 3 shows that a 0.5-mrad divergence (an ~2× beam expansion for a 1-mr beam) produces almost no added error in the measurements, yet it will decrease the background counts by a factor of ~4. The saturation-induced error for a 10× beam expansion of a 100-mJ beam produces a temperature error of only 1.1 K and a wind error of less than 1 m/s (depending on wind technique used), which is comparable to the rest of the system error. These results imply that semidiurnal and diurnal wind and temperature meaasurements are possible without a significant increase in the overall measurement error. Note, however, that measurements of the Na density (which use the absolute strength of the cross section) will be in error when saturation occurs.

A comparison of the errors for the two wind techniques shows that the present wind technique (W_1) is a nearly symmetric measurement about f_a and is much less sensitive to frequency and temperature errors than the second technique (W_2), which relies on a nonsymmetric measurement. This is particularly evident in the sensitivity of W_2 to temperature errors [~1.3 (m/s)/K]. This strong dependence of the wind velocity on the temperature implies that several iterations between the two lookup tables $T(R_T, v_R)$ and $v_R(R_{W_2}, T)$ would need to be performed for self-consistent results.

The W_2 technique does have a distinct advantage over W_1 because one can significantly reduce density variations without averaging if the laser can be tuned on a shot-to-shot basis. Thus, although W_2 is not as accurate as W_1 at the peak of the Na layer, it has the potential to be insensitive to density variations and thus can provide a more accurate measurement over the entire layer with a greater temporal resolution. These errors can be significantly reduced if the data are postprocessed,[16] but they cannot be eliminated. In addition, no effort was made to optimize the frequency used for the wind measurement for the W_2 technique. Optimizing this frequency should decrease the measurement sensitivity to temperature that is the major component of the overall error.

6. Conclusion

A systematic method for the determination of the accuracy of resonance–fluorescence lidar systems has been presented. Furthermore, a general procedure to determine the backscatter cross section that incorporates intensity, divergence, and magnetic-field effects was developed and applied to a specific system. For Na narrowband resonance–fluorescence lidar systems, significant saturation can occur, but the system will still yield accurate measurements, which leads to the prospect of daytime wind and temperature measurements to detect semidiurnal and diurnal effects. The sensitivity of the W/TL system to errors is critically dependent on the choice of the operating point and can vary widely for the same system at differing operating points. Current operational systems are nearly shot-noise limited for both tempera-

Table 4. Total System Error for Each Measurement Technique and the Number of Photons Required to Produce the Same Error as the Total System Error[a]

	Temperature Uncertainty		Wind Uncertainty			
Pulse Characteristics	Error in T (K)	N_{f_a}	Error in W_1 (m/s)	N_{f_a}	Error in W_2 (m/s)	N_{f_a}
35 mJ and 1 mrad	0.53	~226,000	1.01	~12,400	2.01	~53,900
35 mJ and 0.5 mrad	0.54	~226,000	1.01	~12,400	2.01	~53,900
100 mJ and 1 mrad	0.53	~226,000	1.01	~12,400	2.01	~53,900
100 mJ and 0.1 mrad	1.22	~43,000	1.2	~9,300	2.51	~34,600

[a] Calculated for 7-ns pulses at 92 km with $\Delta t = 60$ s.

tures and winds when weighted-averaging techniques are used to minimize errors from density fluctuations. Acousto-optic techniques are being developed that can reduce these errors without one's having to resort to averaging; such developments should provide the potential for better temporal resolution.

Appendix A: Summary of Na Spectroscopy

To understand saturation and optical-pumping effects in Na, it is necessary to understand the electron eigenstates and allowed transitions that form the Na D_2 line. The D_2 line of the Na emission has a nominal wavelength of 589.158 nm and is formed by transitions from the $^3P_{3/2}$ excited state to the $^3S_{1/2}$ ground state. It has a natural lifetime τ_{Na} of 16.40 ± 0.03 ns and an oscillator strength of 0.6357 ± 0.0011.[17] When hyperfine interactions from nuclear–electron spin coupling are included, each of these two states is split. The $^3S_{1/2}$ ground state splits into two levels separated by 1771 MHz, with total angular momentum quantum numbers of f = 1, 2 (see Fig. 6). Because the $^3P_{3/2}$ upper state has higher angular momentum, it splits into four hyperfine states, with total angular momentum quantum numbers of $F = 0$, 1, 2, 3. Finally, the geomagnetic field will Zeeman–split each hyperfine state into $2F + 1$ substates. Each Zeeman substate is designated by its magnetic quantum number m_F, where $-F \le m_F \le F$. For the magnitude of the Earth's magnetic field over Urbana, Illinois, the Zeeman separation is at most 1.6 MHz.

Of the 1431 possible transitions, only 54 satisfy the selection rules for dipole radiation: $\Delta F < 2$, $\Delta m_F < 2$, and if $\Delta F = 0$ then $\Delta m_F \neq 0$.[18] Although transitions of higher order are possible, the strengths of these transitions are negligible compared with the dipole terms.[19]

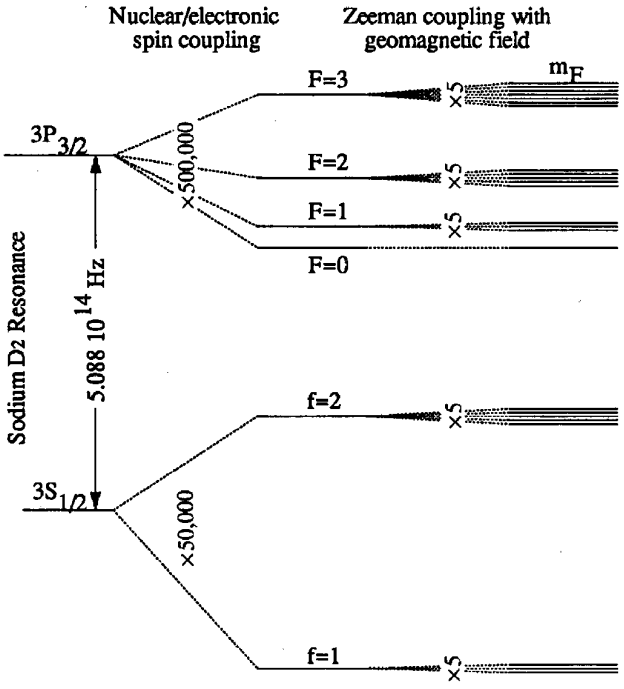

Fig. 6. Energy levels that compose the Na D_2 transition. Numbers preceded by '×' indicate the magnifications of the energy difference.

The geomagnetic field provides each atom with a preferred axis of orientation along the field lines, and this leads to a definite polarization structure for the atoms. Transitions for which $\Delta m_F = 0$ emit along the axis of orientation (π); transitions for $\Delta m_F = +1$ emit clockwise circular polarization along the axis (σ^+); transitions for $\Delta m_F = -1$ emit counterclockwise circular polarization along the axis (σ^-).

Exact treatment for arbitrary excitation, detection, and polarization must include all 24 states and 54 transitions through a density-matrix approach. Often, assumptions can be made that reduce the complexity of this approach. In the atmosphere, the excitation beam is spectrally broad with respect to the spread of the Zeeman states. In addition, it contains a nearly uniform combination of all three polarization states. Under these conditions, Zeeman levels may be grouped by their total angular momentum quantum numbers, f or F. Transition strengths for each group are determined by summation over the individual Zeeman transition strengths (which are determined by the Hanle effect). The states and transitions defined under this approximation are shown in Fig. 7.

1. Doppler-Free Features in Na Vapor

The Na-vapor cell was fabricated by placement of solid Na into an evacuated glass tube. After the cell was sealed, a temperature-dependent equilibrium forms between Na in the solid phase and that in the vapor phase. The concentration of Na vapor in the cell at equilibrium is determined by the temperature of the cell and the vapor pressure of Na: higher temperatures increase the concentration of sodium vapor. For low levels of laser excitation, this vapor is in thermal equilibrium with the walls of the cell.

To understand the spectroscopy of this vapor, it is convenient to discuss the response for each individual velocity ensemble within the Boltzmann distribution. First, examine the excitation for a general ensemble with nonzero velocity in the positive z direction. As the frequency of the counterpropagating laser beams is swept through the Na resonance, the beam traveling in the positive z direction will interact with each of the six hyperfine transitions of this ensemble, but, because the ensemble is moving with velocity v_z in the direction of light propagation, the fluorescence in the laboratory (rest) frame is downshifted from the zero-velocity fluorescence by v_z/λ. The response of this velocity ensemble that results from the other beam is similar, except that the response is now upshifted by v_z/λ. Thus, each velocity ensemble will, in general, generate 12 narrow spikes of fluorescence, with ensembles of higher velocity responding farther away from the zero-velocity transition frequencies. Because we have no way of distinguishing the response from individual velocity ensembles, we detect the sum of the fluorescence of all velocity ensembles, weighted by the Boltzmann distribution of each ensemble.

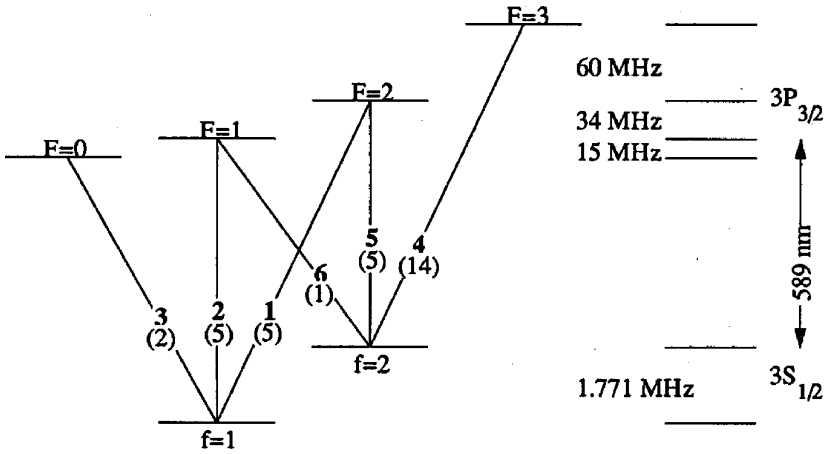

Fig. 7. Six-transition model used for the vapor-cell calibration and saturation simulations. The number of the transition is shown in boldface. The relative oscillator strength in the absence of a magnetic field is shown in parentheses. Upper states are designed by the total angular momentum quantum number F, and ground states are designated by f.

Except for the factor of 2 that results from two beams (instead of one), this sum would generate the usual linear cross section described by Eq. (5).

The above description is true for most velocity ensembles in the vapor cell. However, some velocity ensembles will have special excitations. For the stationary velocity ensemble, no Doppler shift will occur, and, if properly tuned, both probing laser beams excite transitions from the same ground state. If the intensity of each of these two beams is strong enough, the ground state will be depleted, and the fluorescence response for this velocity ensemble will be reduced from the linear value. This effect will appear as Lamb dips in the linear fluorescence spectrum that are centered around the zero-velocity transition frequencies (both beams excite the same transition) and around the midpoints between these transitions (the beams excite different transitions from the same ground state). Finite transition and laser linewidths serve to blend these dips, which forms the Doppler-free features at f_a and f_c. Our description is further complicated by the fact that each transition saturates according to its strength, which implies that a numerical simulation is necessary to fully describe the Doppler-free features.

One more special excitation exists. Some ensembles of atoms will have a z velocity such that atoms interacting with that beam are upshifted to one of the D_{2a} transitions, while the same set of atoms interacts with the other beam downshifted to a D_{2b} transition (and vice versa). For this ensemble, atoms are simultaneously excited from both ground-state manifolds. Hence, optical pumping cannot occur and the fluorescence is increased. This process generates the crossover feature around the midpoint between the D_{2a} and D_{2b} resonances.

2. Hanle Effect

The Hanle effect is the depolarization of the radiation characteristics of an atom in the presence of an external magnetic field. An external magnetic field **B** creates an axis of symmetry for the atom (z axis in a spherical coordinate system). Propagation of the outgoing laser field is denoted by k, and the general elliptic polarization state is then described with respect to a set of polarization axes θ_0 and ϕ_0, as shown in Fig. 8, where ϕ_0 is confined to the x–y plane. This special coordinate system will be referred to as the natural coordinate system to differentiate it from the laboratory system in which the measurements are defined.

For an accurate representation of the Na fluorescence, one must solve a rate equation for the density matrix of the excited states $\rho_{mm'}$ of the scattering process[20] given by

$$\frac{d\rho_{mm'}}{dt} = -i[V, \rho]_{mm'} - \sum_{m_1 m_1'} \Gamma_{mm'}{}^{m_1 m_1'} \rho_{m_1 m_1'} + F_{mm'}, \tag{A1}$$

where V is the energy operator of the interaction between the atom and the external magnetic field, Γ describes the relaxation (emission) process, and $F_{mm'}$ describes the excitation (absorption) of the atoms by the external light source. This equation may be cast into a more useful form (separating the geometry, symmetry, and selection rules from the dynamics of the density matrix) if we expand the equation in terms of spherical irreducible tensor operators.[21] The resulting rate equation for each component of the density matrix is

$$\frac{d\rho_q{}^k}{dt} = i\mu_B g q B \rho_q{}^k - \gamma_k \rho_q{}^k + F_q{}^k, \tag{A2}$$

where μ_B is the Bohr magneton, g is the Landè g factor for the excited state, and B is the geomagnetic-field strength. The term $\rho_0{}^0$ is proportional to the population of the excited level, $\rho_q{}^1$ are dipole terms and are proportional to the average value of the qth circular component (defined in the same manner as the spherical polarization vectors given below) of the total angular momentum of the excited atoms, and $\rho_q{}^2$

are quadrupole terms. The indices have the ranges $0 \le k \le 2$ and $-k \le q \le k$ such that higher-order terms are neglected. We obtain the solution to Eq. (A2) by using the following assumptions:

1. The incident light bandwidth is much broader than the Zeeman splitting of the excited state (geomagnetic Zeeman splitting for the $F = 3$ state is 1.6 MHz).
2. Excitation occurs only from the various ground-state sublevels.
3. Interference terms between sublevels of the excited state and nondiagonal elements of the ground-state density matrix are neglected.
4. The magnetic field is weak.
5. The sublevels of the ground state are equally populated.
6. The receiver response is broad with respect to the full sodium resonance.

With these assumptions, the scattered field for each hyperfine transition is given by[22]

$$R_{fF}(\hat{e}, \hat{u}, B) = R_0(-1)^{I-f-J_0'}A_{fF}[f][F]^2 \times \begin{Bmatrix} J & F & I \\ f & J_0 & 1 \end{Bmatrix}^2 \sum_{k,q} (-1)^{k+q} \begin{Bmatrix} 1 & 1 & k \\ J & J & J_0' \end{Bmatrix} \times \begin{Bmatrix} J & J & k \\ F & F & I \end{Bmatrix} \begin{Bmatrix} 1 & 1 & k \\ F & F & f \end{Bmatrix} \times \Phi^k_{-q}(\hat{e})\Phi^k_q(\hat{u})(1 + iqg_F\mu_B\tau B/\hbar)^{-1}, \tag{A3}$$

where R_0 is a constant proportional to the reduced matrix elements $|(J\|d\|J_0)|^2|(J\|d\|J_0')|^2$, A_{fF} accounts for different excitation rates for each hyperfine transition, $[f] \equiv 2f + 1$, J and J_0' are the total spin quantum numbers of the upper and lower states ($3/2$ and $1/2$ respectively), I is the nuclear spin quantum number ($3/2$), $\{\cdots\}$ denotes the Wigner $6j$ symbol, $\hat{e}$ and $\hat{u}$ are the polarization unit vectors of the exciting and detected light, respectively, g_F is the Landè g factor for the excited state ($2/3$), $\tau = 16.40 \pm 0.03$ ns is the lifetime of the Na atom, B is the geomagnetic-field strength in tesla, μ_B is the Bohr magneton and is 9.27408×10^{-24} J T^{-1}, and $\hbar = 1.054589 \times 10^{-34}$ J s. The Φ terms in Eq. (A3) are a modified version of those given by D'Yakonov[20]:

$$\Phi^k_q(\hat{e}) = (-1)^q(2k + 1)^{1/2} \sum_{q_1 q_2} (-1)^{q_2}\hat{e}_{q_1}\hat{e}_{q_2}^* \times \begin{bmatrix} 1 & 1 & k \\ q_1 & -q_2 & -q \end{bmatrix}, \qquad -1 \le q_1, q_2 \le 1, \tag{A4}$$

where $\hat{e}_q$ is the expansion of the polarization vector in terms of the spherical polarization basis vectors given by

$$\hat{e}_{\pm 1} = \mp \frac{1}{\sqrt{2}}(\hat{x} \pm i\hat{y}), \qquad \sigma^{\pm} \text{ polarizations},$$
$$\hat{e}_0 = \hat{z}, \qquad \pi \text{ polarization}. \tag{A5}$$

For the general elliptic polarization shown in Fig. 8 we have

$$\hat{e} = \cos\gamma\hat{x}' + i\sin\gamma\hat{y}', \qquad -\pi/4 \le \gamma \le \pi/4,$$
$$\hat{x}' = \cos\beta\hat{\theta}_0 + \sin\beta\hat{\phi}_0, \qquad 0 \le \beta \le \pi,$$
$$\hat{y}' = \sin\beta\hat{\theta}_0 + \cos\beta\hat{\phi}_0, \tag{A6}$$

where $\gamma = 0$ corresponds to linear polarization and $\gamma = \pm\pi/4$ corresponds to circular polarization. For a wave propagating in the direction (θ, ϕ), as defined above,

$$\hat{\theta}_0 = \cos\phi\cos\theta\hat{x} + \sin\phi\cos\theta\hat{y} - \sin\theta\hat{z},$$
$$\hat{\phi}_0 = \sin\phi\hat{x} + \cos\phi\hat{y}.$$

Finding the projection of $\hat{e}$ on the basis vectors that are defined in Eq. (A5) we obtain

$$\hat{e}_{\pm 1} = \mp \frac{1}{\sqrt{2}}[\cos\beta(\cos\gamma\cos\theta \mp \sin\gamma) - i\sin\beta(\sin\gamma\cos\theta \mp \cos\gamma)]\exp(\pm i\phi),$$
$$\hat{e}_0 = -(\cos\gamma\cos\beta - i\sin\gamma\sin\beta)\sin\theta. \tag{A7}$$

Thus Φ can be written as

$$\Phi^0_0(\hat{e}) = -1/\sqrt{3},$$
$$\Phi^1_0(\hat{e}) = 1/\sqrt{2}\sin(2\gamma)\cos\theta,$$
$$\Phi^1_{\pm 1}(\hat{e}) = \mp 1/2\sin(2\gamma)\sin\theta\exp(\pm i\phi),$$
$$\Phi^2_0(\hat{e}) = -1/\sqrt{6}[1 - (3/2)[1 + \cos(2\beta)\cos(2\gamma)]\sin^2(\theta)],$$
$$\Phi^2_{\pm 1}(\hat{e}) = \pm 1/2[[1 + \cos(2\beta)\cos(2\gamma)]\cos\theta \pm i\sin(2\beta)\cos(2\gamma)]\sin\theta\exp(\pm i\phi),$$
$$\Phi^2_{\pm 2}(\hat{e}) = 1/2[\cos(2\beta)\cos(2\gamma) - (1/2)[1 + \cos(2\beta)\cos(2\gamma)] \times \sin^2(\theta) \pm i\sin(2\beta)\cos(2\gamma)\cos\theta]\exp(\pm i2\phi). \tag{A8}$$

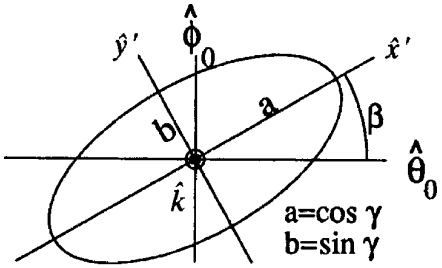

Fig. 8. Geometry for the coordinate transformation required to determine the Hanle effect.

Normally lidar receivers are unpolarized. An unpolarized receiver is the sum of two orthogonal polarizations. Taking the sum of Eq. (A8) for (β, γ) and for $(\beta + \pi/2, \gamma)$ gives the following solution for the receiver-geometry dependence in the natural system:

$$\Phi_0^0(\hat{u}) = -2/\sqrt{3}, \qquad \Phi_{0,\pm1}^1(\hat{u}) = 0,$$
$$\Phi_0^2(\hat{u}) = -2/\sqrt{6}[1 - 3/2\,\sin^2(\theta_r)]$$
$$\Phi_{\pm1}^2(\hat{u}) = \pm\sin(\theta_r)\cos(\theta_r)\exp(\pm i\phi_r),$$
$$\Phi_{\pm2}^2(\hat{u}) = -1/2\,\sin^2(\theta_r)\exp(\pm i2\phi_r). \tag{A9}$$

Thus the polarization terms in the solution for a linearly polarized transmitter and an unpolarized receiver are

$$\Phi_0^0(\hat{e})\Phi_0^0(\hat{u}) = 2/3,$$
$$\Phi_{0,\mp1}^1(\hat{e})\Phi_{0,\pm1}^1(\hat{u}) = 0,$$
$$\Phi_0^2(\hat{e})\Phi_0^2(\hat{u}) = (1/3)[1 - (3/2)\sin^2(\theta_r)][1 - (3/2) \times [1 + \cos(2\beta)]\sin^2(\theta_t)],$$
$$\Phi_{\mp1}^2(\hat{e})\Phi_{\pm1}^2(\hat{u}) = -(1/2)\sin(\theta_r)\cos(\theta_r)\sin(\theta_t) \times \{[1 + \cos(2\beta)]\cos(\theta_t) \mp i\,\sin(2\beta)\} \times \exp[\pm i(\phi_r - \phi_t)],$$
$$\Phi_{\mp2}^2(\hat{e})\Phi_{\pm2}^2(\hat{u}) = -(1/4)\sin^2(\theta_r)\{\cos(2\beta) - (1/2) \times [1 + \cos(2\beta)]\sin^2(\theta_t) \mp i\,\sin(2\beta) \times \cos(\theta_t)\}\exp[\pm i2(\phi_r - \phi_t)]. \tag{A10}$$

We must now obtain the angles θ, ϕ, and β that were defined for the natural coordinate system of Fig. 9 in terms of the corresponding angles in the laboratory coordinate system. Referring to Fig. 9, we take a geographical (east, north, and vertical) system and define the magnetic unit vector $\hat{b}$ to make an angle $I + \pi/2$ with the vertical axis $\hat{v}$ and an angle D with the north axis $\hat{n}$. The propagation vector $\hat{k}$ makes an angle χ with the vertical axis and an angle Ψ with the east axis. In a manner completely analogous to the definition of the polarization-vector rotation angle in the natural coordinate system we define the corresponding angle α. Then we can rotate the coordinates through the Euler angles $[-D, -(I + \pi/2), 0]$ to put $\hat{b}$ on the z axis. This gives a rotation matrix

$$\mathbf{V}_n = \begin{bmatrix} \cos D & -\sin D & 0 \\ -\sin D \sin I & -\cos D \sin I & -\cos I \\ \sin D \cos I & \cos D \cos I & -\sin I \end{bmatrix} \mathbf{V}_l, \tag{A11}$$

which is to be applied to the vectors $\hat{k}$, $\hat{b}$, and $\hat{p}$.

We can now use vector relations to obtain expressions for the desired angles. The angle θ is found from $\cos\theta = \hat{k} \cdot \hat{b}$. $\hat{\phi}_0$ is given by $\hat{\phi}_0 = \hat{k} \times \hat{b}/\sin\theta$. Because $\hat{\phi}_0$ is perpendicular to $\hat{b}$, it is easy to show that $\sin\phi = \hat{x}\hat{\phi}_0$. Finally, because ϕ_0 is perpendicular to $\hat{k}$, we can show that $\sin\beta = \hat{p}\hat{\phi}_0$.

At the University of Illinois laser radar installation the magnetic field in the vicinity of the vapor cell has a declination of $-40°$ (measured at the location of the vapor cell), an estimated inclination of 70°, and an estimated field strength of 56.6 μT.[23] If we normalize the oscillator strengths to the $f = 1$, $F = 0$ transition with a value of 2 (as this transition does not depend on the magnetic field), the relative oscillator strengths are obtained with the ratios 5:5.5:2:15.68:5:0.98, when the magnetic field is zero. The results of the above analysis for the west-going beam into the Na-vapor cell for vertical and horizontal polarizations gives the relative oscillator strengths shown in Table 5. It is important to note that these values will vary from location to location, including locations in the atmosphere. With these same computations, the atmospheric oscillator-strength ratios over Urbana have been determined to be 5:5.48:2:15.64:5:0.98. If ignored, these changes result in a derived temperature bias of 1.4 K and a derived wind-velocity bias of 0.7 m/s. The computations shown in this section must be recomputed for each lidar site, beam direction, and polarization for which this technique is used because of the large variations in magnetic-field direction around the globe.

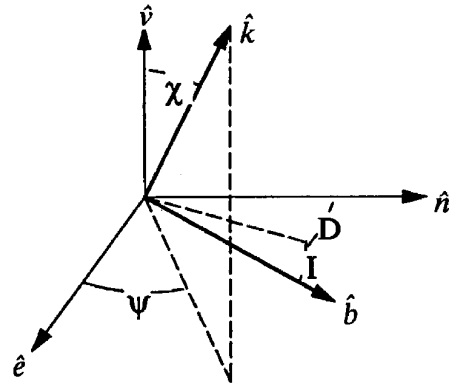

Fig. 9. Relation of $\hat{k}$ and $\hat{b}$ to geographical coordinates.

Appendix B: Simulations

To properly calibrate the vapor cell and assess the effects of saturation and optical pumping in the atmosphere, one must use a model for the sodium D_2 line. A rate-equation approach is valid for pulse lengths of the order of the transition lifetime (~16 ns).

Table 5. Relative Oscillator Strengths for a Beam Traveling West through the Vapor Cell

Transition	Horizontal	Vertical	Ratio (H/V)
1	5	5	1
2	5.76	5.19	1.11
3	2	2	1
4	16.55	14.62	1.13
5	5	5	1
6	0.97	0.99	0.98

For pulse durations significantly less than this (high peak intensity), a density-matrix approach must be used owing to the importance of Rabi oscillations.[24,25]

1. Six-Level Rate Equations

If the spectrum of the exciting light is broad with respect to the Zeeman splittings and if it comprises a uniform mixture of π, σ^+, and σ^- polarizations, the 24-state model of the Na atom D_2 resonance can be approximated by the six-state model discussed in Appendix A. The rate equations that describe a single position and velocity ensemble of atoms under this model are

$$\begin{aligned}
\frac{dN_{F_0}}{dt} &= \xi_3(t)\left(N_{f_1} - \frac{g_{F_0}}{g_{f_1}} N_{F_0}\right) - \frac{N_{F_0}}{\tau_3} - \frac{(N_{F_0} - 0)}{\tau_C},\\
\frac{dN_{F_1}}{dt} &= \xi_2(t)\left(N_{f_1} - \frac{g_{F_1}}{g_{f_1}} N_{F_1}\right) + \xi_6(t)\left(N_{f_2} - \frac{g_{F_1}}{g_{f_2}} N_{F_1}\right)\\
&\quad - \frac{N_{F_1}}{\tau_2} - \frac{N_{F_1}}{\tau_6} - \frac{(N_{F_1} - 0)}{\tau_C},\\
\frac{dN_{F_2}}{dt} &= \xi_1(t)\left(N_{f_1} - \frac{g_{F_2}}{g_{f_1}} N_{F_2}\right) + \xi_5(t)\left(N_{f_2} - \frac{g_{F_2}}{g_{f_2}} N_{F_2}\right)\\
&\quad - \frac{N_{F_2}}{\tau_1} - \frac{N_{F_2}}{\tau_5} - \frac{(N_{F_2} - 0)}{\tau_C},\\
\frac{dN_{F_3}}{dt} &= \xi_4(t)\left(N_{f_2} - \frac{g_{F_3}}{g_{f_2}} N_{F_3}\right) - \frac{N_{F_3}}{\tau_4} - \frac{(N_{F_3} - 0)}{\tau_C},\\
\frac{dN_{f_1}}{dt} &= -\xi_3(t)\left(N_{f_1} - \frac{g_{F_0}}{g_{f_1}} N_{F_0}\right) - \xi_2(t)\left(N_{f_1} - \frac{g_{F_1}}{g_{f_1}} N_{F_1}\right)\\
&\quad - \xi_1(t)\left(N_{f_1} - \frac{g_{F_2}}{g_{f_1}} N_{F_2}\right) + \frac{N_{F_0}}{\tau_3} + \frac{N_{F_1}}{\tau_2}\\
&\quad + \frac{N_{F_2}}{\tau_1} - \frac{\left(N_{f_1} - \dfrac{g_{f_1}}{g_{f_1} + g_{f_2}}\right)}{\tau_C},\\
\frac{dN_{f_2}}{dt} &= -\xi_6(t)\left(N_{f_2} - \frac{g_{F_1}}{g_{f_2}} N_{F_1}\right) - \xi_5(t)\left(N_{f_2} - \frac{g_{F_2}}{g_{f_2}} N_{F_2}\right)\\
&\quad - \xi_4(t)\left(N_{f_2} - \frac{g_{F_3}}{g_{f_2}} N_{F_3}\right) + \frac{N_{F_1}}{\tau_6} + \frac{N_{F_2}}{\tau_5}\\
&\quad + \frac{N_{F_3}}{\tau_4} - \frac{\left(N_{f_2} - \dfrac{g_{f_2}}{g_{f_1} + g_{f_2}}\right)}{\tau_C}. \qquad \text{(B1)}
\end{aligned}$$

In these equations, $N_x(t, v_R, \mathbf{r})$ represents the fraction of the population in state x at time t for the ensemble of atoms with radial velocity v_R and lateral position $\mathbf{r}$, where the functional dependence was suppressed for brevity. For Appendix B, the use of the term v_R denotes both the radial-wind velocity in the atmosphere and the velocity of the Na atoms within the vapor cell. The degeneracy of state x is g_x, and $\xi_y(t)$, which is the excitation for this ensemble, is given by

$$\xi_y(t, v_R, \mathbf{r}) = \frac{1}{hf}\int df \sigma_y(f) I_1(f, t, v_R, \mathbf{r}). \qquad \text{(B2)}$$

The lifetime of each transition τ_y is related by the strength of transition y, S_y, to the lifetime of the D_2 resonance by

$$\tau_y = \tau_{\mathrm{Na}} \frac{\sum S_y}{S_y}. \qquad \text{(B3)}$$

The single fitted parameter τ_C is related to the rate at which atoms cross the area of the beam. It represents a replenishing rate of atoms entering the beam from the surrounding equilibrium. In the atmosphere, the beam radius is large compared with expected horizontal wind velocities, and $\tau_C \to \infty$.

The line shape of each transition, $\sigma_y(f)$, is Lorentzian:

$$\sigma_y(f) = \frac{1}{4\pi\varepsilon_0}\frac{\pi q_e^2}{m_e c} S_{\mathrm{os}} \frac{S_y}{\sum S_y}\frac{1}{2\pi}\frac{\Delta f_y}{(f - f_y)^2 + \left(\dfrac{\Delta f_y}{2}\right)^2}, \qquad \text{(B4)}$$

where f_y is the center frequency of transition y and S_{os} is the fraction of the unit oscillator strength for the entire D_2 line. The spectral FWHM of each transition is determined by

$$\Delta f_y = \frac{\Delta\omega_{\mathrm{FWHM}}}{2\pi} = \frac{1}{\tau_y \pi}. \qquad \text{(B5)}$$

The excitation intensity $I_1(f, t, v_R, \mathbf{r})$ will vary with different excitations but is assumed to be Gaussian both spectrally and spatially with a time dependence $\phi(t)$. For a single beam, the excitation intensity will be

$$\begin{aligned}
I_1(f, t, v_R, \mathbf{r}) &= \frac{1}{(2\pi)^{1/2}\sigma_r(z)} \exp\left(-\frac{|\mathbf{r}|^2}{2\sigma_r^2(z)}\right)\left(\frac{1}{(2\pi)^{1/2}\sigma_1}\right)\\
&\quad \times \exp\left\{-\frac{\left[f - \left(f_1 + f_0\dfrac{v_R}{c}\right)\right]^2}{2\sigma_1^2}\right\}\phi(t). \qquad \text{(B6)}
\end{aligned}$$

Here the lateral beam width $\sigma_r^2(z)$ is defined in terms of the full angle divergence θ by

$$\sigma_r(z) = \sigma_0 + z\frac{\theta}{2}. \qquad \text{(B7)}$$

In the vapor cell, the second term in Eq. (B7) is ignored. Spectrally, the excitation has rms width σ_1

centered at the laser tuning frequency f, which is Doppler shifted by $-v_R/\lambda$. For cw excitation, the intensity time dependence $\phi(t)$ is only the spatially integrated beam intensity. The pulse excitation is the total energy in the pulse E multiplied by a normalized temporal function that represents the temporal pulse shape. For the pulse shape assumed in this work, the pulse-intensity time dependence is[13]

$$\phi(t) = E\,\frac{t}{2t_r^2}\exp\left\{-\frac{t^2}{4t_r^2}\right\}, \tag{B8}$$

where t_r is defined in terms of the rms pulse length as

$$t_r = \frac{\Delta t_{\mathrm{rms}}}{(2-\pi/2)^{1/2}}. \tag{B9}$$

These rate equations are used to simulate both saturation and optical-pumping effects in the atmosphere, as well as the Doppler-free spectroscopy of the vapor cell. We note that, although a specific temporal envelope is used, the results are relatively independent of the pulse shape as long as rms values are used.[13]

2. Saturation and Optical Pumping in the Six-Level Model

Typically, saturation effects are described with atoms that have only two energy levels. When an atom that is originally in the ground state is excited at the transition frequency, the probability of the atom being in the ground state is reduced while the probability of the atom being in the upper state is increased. This reduces the probability for the atom to absorb another photon and causes a bleaching of the absorption. Moreover, the finite probability of the atom being in the upper state increases the probability of stimulated emission. This is particularly deleterious to resonance lidars because the stimulated photon travels along the excitation beam, i.e., travels opposite to the direction of the detector. These nonlinear effects depend on the intensity of the beam at the Na layer. Because atmospheric transmittance may vary, it is difficult to ascertain the exact intensity of the beam at the layer, which in turn makes determination of the layer saturation difficult.

When an atom with multiple ground states is excited with a narrow-bandwidth source, optical pumping can also serve to reduce the effective-fluorescence cross section (see Subsection 3.B).

To determine the percent saturation for a given pulse in the atmosphere, Eq. (B1) is solved for each velocity ensemble and each location in the beam under the assumption of isolated conditions ($\tau_C \to \infty$). The excitation intensity is computed with Eqs. (B6)–(B9). The total saturated response is computed from the results of all ensembles as

$$R_{\mathrm{Sat}}(f_1) = \int \mathrm{d}v_R \int \mathrm{d}\mathbf{r} \int \mathrm{d}t \sum_x \frac{N_{F_x}(t, v_R, \mathbf{r})}{\tau_{F_x}}, \tag{B10}$$

where τ_{F_x} is the parallel combination of all decay from state F_x. The linear response is determined in similar fashion except that the lower-state populations, N_{f_1} and N_{f_2}, are held constant at a Boltzmann distribution for the duration of the simulation. Saturation is defined as the percent decrease in the saturated response compared with the linear response.

3. Vapor-Cell Simulation and Absolute Frequency Calibration

The Doppler-free fluorescence response of Na vapor is produced by simultaneous excitation of the vapor with two counterpropagating beams, which produces the Doppler-free features shown in Fig. 10. This introduces two terms into the excitation intensity, one for the leftward-traveling beam, the other for the rightward-traveling beam. The driving excitation then becomes

$$\xi_y(v_R, \mathbf{r}) = \frac{1}{hf}\int \mathrm{d}f\sigma_y(f)[I_1(f, v_R, \mathbf{r}) + I_1(f, -v_R, \mathbf{r})]. \tag{B11}$$

The vapor-cell fluorescence response may be determined from the steady-state solutions of Eqs. (B1). Solutions are computed for all positions and velocity

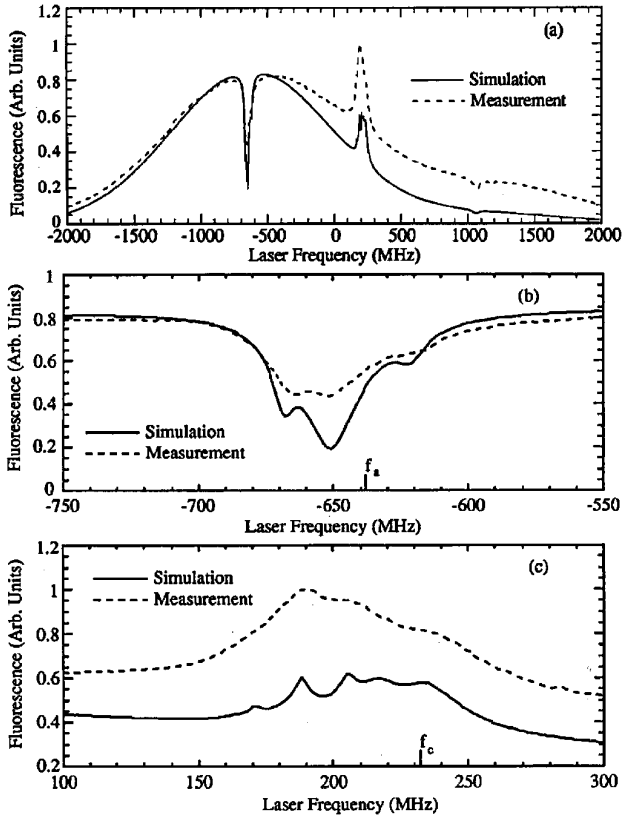

Fig. 10. (a) Data for the model of the Na Doppler-free features compared with the experimental data. (b) Expanded view near peak f_a. (c) Expanded view near the crossover f_c. The fit between the experimental data and the model provides calibration to within ±2 MHz.

ensembles to determine the total fluorescence:

$$\text{Fluorescence}(f_1) = \int dv_R \int d\mathbf{r} \sum_x \frac{N_{F_x}(v_R, \mathbf{r})}{\tau_{F_x}}. \quad \text{(B12)}$$

Figure 10 shows the comparison between the experimental fluorescence response and the response determined from the simulation through the use of Eqs. (B1)–(B11). Figure 10(a) shows the entire fit. Figures 10(b) and 10(c) show the detail within the peak and the crossover transitions, from which the absolute laser frequency can be determined to ±2 MHz. The only free parameter in the simulation is τ_C, the beam traversal rate, which was chosen to minimize the difference between the vapor-cell simulation and its measurements.

The difference in the background fluorescence near the D_{2b} peak is from the lack of an equilization term between the two ground-state manifolds that is caused by the collisional and boundary effects within the vapor cell. Without this term, the simulation tends to overestimate the effects of optical pumping for the D_{2b} peak, which decreases the overall fluorescence relative to what is experimentally measured. Discrepancies also exist within the Doppler-free features shown in Figs. 10(b) and 10(c). These differences are probably due to the relatively broadband excitation that is assumed in the six-state model. The cw laser that excites the vapor cell has an rms linewidth of approximately 500 kHz. This linewidth is narrower than the separation of the individual Zeeman splittings of the hyperfine transitions and leads to the necessity of a more accurate model of the vapor-cell response that uses the full 24-state description of the Na atoms.[24] Finally, the best-fit result for τ_C was approximately 1 order of magnitude larger than was expected for the cell temperature and beam diameter; this result reflects that several effects that are not included in this model are important for exact agreement. However, the six-level rate-equation simulation is sufficient because the absolute laser frequency error does not dominate the total system error.

Once the absolute laser frequency is known, an automated tuning algorithm defines the four lock frequencies from the Doppler-free features of the vapor cell and a 0.5-m confocal Fabry–Perot interferometer. The frequency f_a is defined to be the point at which the vapor-cell response rises above the minimum of the D_{2a} Lamb dip on the high-frequency side by 15% of the depth of the dip [see Fig. 10(b)]. The frequency f_c is defined to be at the point at which the vapor-cell response drops to 85% of its maximum value on the high-frequency side of the crossover feature [see Fig. 10(c)]. Each time a wind measurement is made, a Fabry–Perot interferometer with a spectral range of 150 MHz is tuned through four reconance peaks to produce the 600-MHz shift from f_a to generate f_+ and f_-. The fitted data yield absolute frequencies for the tuning algorithm of $f_a = -638 \pm 2$ MHz, $f_c = 232 \pm 2$ MHz, $f_+ = -1238 \pm 2$ MHz, and $f_- = -38 \pm 2$ MHz.

Appendix C: Derivation of Density Variations

Here we present a derivation of the effects of density variations on temperature and wind measurements. We start with a modified form of Eq. (3)

$$R(z, t, \Delta t) = \frac{N_{f_1}(z, t + \Delta t)}{N_{f_2}(z, t)} = \frac{\sigma_{\text{eff}}(f_1)\rho_s(z, t + \Delta t)}{\sigma_{\text{eff}}(f_2)\rho_s(z, t)}, \quad \text{(C1)}$$

that suppresses the functional dependence of σ_{eff} on the various system parameters and replaces the measurement interval t by the integration time Δt. This approximation is valid as long as the dead time that is required between profiles to write the data and to tune the laser is much less that the integration time Δt, as it is in our W/TL system. The density profile $\rho_s(z, t + \Delta t)$, may be written as

$$\rho_s(z, t + \Delta t) = \bar{\rho}_s + \rho_s', \quad \text{(C2)}$$

where $\bar{\rho}_s$ is the mean density profile and ρ_s' is a perturbation from the mean over the time interval Δt. The functional dependence of both terms has been suppressed for clarity. Using Eq. (C2) in Eq. (C1), we can write the ratio as

$$R \approx R\left(1 + \frac{\rho_s'}{\bar{\rho}_s}\right), \quad \text{(C3)}$$

where R is the mean ratio and the variation from the mean is

$$\frac{\Delta R}{R} \approx \frac{\rho_s'}{\bar{\rho}_s}, \quad \text{(C4a)}$$

or

$$R' \approx r_s, \quad \text{(C4b)}$$

where $R' = \Delta R/R$ is the relative perturbation in the ratio caused by density fluctuations and $r_s = \rho_s'/\bar{\rho}_s$ is used to be consistent with Ref. 15. Equations (C4a) and (C4b) are equivalent to Eq. (20) of Ref. 1.

The relative perturbations in the Na density r_s can be related to the relative atmospheric perturbations r_a with[5]

$$r_s = \frac{1}{(\gamma - 1)}[1 - (z - z_0)\gamma H/\sigma_0^2]r_a, \quad \text{(C5)}$$

where $r_a = \rho_a'/\bar{\rho}_a$, σ_0 is the rms thickness of the unperturbed Na layer (~4.2 km), H is the atmospheric scale height (~6 km), z_0 is the centroid height (~92 km), and γ is the ratio of specific heats (1.4). With Eqs. (C4) and (C5), the relative change in the ratio R' is given by

$$R'(z) \approx \frac{1}{(\gamma - 1)}[1 - (z - z_0)\gamma H/\sigma_0^2]r_a. \quad \text{(C6)}$$

The temporal dependence of the relative perturbation in the ratio R' is determined through the use of differentials. For example, the perturbation in a time interval Δt is given by

$$\Delta R'(z, \Delta t) \approx \frac{1}{(\gamma - 1)} [1 - (z - z_0)\gamma H/\sigma_0^2] \frac{\partial r_a}{\partial t} \Delta t. \tag{C7}$$

To find the variance of these perturbations, we square both sides of Eq. (C7), take the expectation, and multiply and divide by the expectation of the square of r_a, $\langle r_a^2 \rangle$:

$$\langle [\Delta R'(z, \Delta t)]^2 \rangle \approx \langle r_a^2 \rangle \frac{\Delta t^2}{(\gamma - 1)^2} [1 - (z - z_0)\gamma H/\sigma_0^2]^2 \times \left[\frac{\left\langle \left(\frac{\partial r_a}{\partial t} \right)^2 \right\rangle}{\langle r_a^2 \rangle} \right]. \tag{C8}$$

The last term in square brackets on the right-hand side of Eq. (C8) is ω_{rms}^2, the rms temporal frequency [see Eq. (38) of Ref. 15]. It is related to the rms temporal period T_{rms} by $T_{\text{rms}} = 2\pi/\omega_{\text{rms}}$. The rms temporal period T_{rms} represents the time over which the random wave field is correlated. For times less than T_{rms}, the random fluctuations are small.

Rewriting Eq. (C8) in terms of T_{rms} and taking the square root of each side we obtain

$$\langle [\Delta R'(z, \Delta t)]^2 \rangle^{1/2} \approx \frac{1}{T_{\text{rms}}} \frac{(2\pi \Delta t)}{(\gamma - 1)} [1 - (z - z_0)\gamma H/\sigma_0^2] \times \langle r_a^2 \rangle^{1/2}. \tag{C9}$$

The correlation time T_{rms} and variance of the relative atmospheric perturbations $\langle r_a^2 \rangle^{1/2}$ have been experimentally measured and the yearly mean values are $T_{\text{rms}} = 44$ min, and $\langle r_a^2 \rangle^{1/2} = 5.6\%$.[15] Note that there is a significant seasonal dependence of these values. Table 6 shows the relative error as a function of integration time Δt and the altitude when the yearly mean values are used. Relative errors as large as 10% occur for 1-min integrations at the bottom side of the layer.

Table 6. Magnitude of the Percent Relative Density Error[a] as a Function of z and the Time Between Profiles Δt

	z				
Δt	84 km	88 km	92 km	96 km	100 km
10 s	1.60	0.968	0.333	0.301	0.936
30 s	4.81	2.90	1.00	0.904	2.81
60 s	9.62	5.81	2.00	1.81	5.62

[a]Relative density error $[\Delta R'(\Delta t)]^2$ calculated with Eq. (C9) for parameter values $\sigma_0 = 4.2$ km, $H = 6$ km, $z_0 = 92$ km, $\gamma = 1.4$, $T_{\text{rms}} = 44$ min, and $\langle r_a^2 \rangle^{1/2} = 5.6\%$.

Optimal averaging can significantly reduce the density fluctuations for both temperature and wind measurements that are calculated with Eq. (C9). Using a temperature measurement as an example, we write R' in terms of weighted density profiles[16]

$$R'(\Delta t) = r_{sp} - r_{sc}, \tag{C10}$$

where

$$r_{sp} = \frac{\alpha r_s(t - 2\Delta t) + r_s(t) + \alpha r_s(t + 2\Delta t)}{1 + 2\alpha}, \tag{C11}$$

$$r_{sc} = \frac{\beta r_s(t - 3\Delta t) + r_s(t - \Delta t) + r_s(t + \Delta t) + \beta r_s(t + 3\Delta t)}{2(1 + \beta)}. \tag{C12}$$

The coefficients α and β ($\alpha = 3/10$ and $\beta = 1/15$) are chosen to equalize the weighted profiles up to terms in $(\Delta t)^4$. The weighted densities then differ by sixth-order and higher terms, with the most significant error term given by

$$R'(\Delta t) \approx \frac{(\Delta t)^6}{32} \frac{\partial r_s^6}{\partial t^6}. \tag{C13}$$

We now rewrite Eq. (C13) in terms of the relative atmospheric perturbations using Eq. (C5):

$$R'(z, \Delta t) \approx \frac{(\Delta t)^6}{32} \frac{1}{(\gamma - 1)} [1 - (z - z_0)\gamma H/\sigma_0^2] \frac{\partial r_a^6}{\partial t^6}, \tag{C14}$$

To estimate the derivative of the atmospheric density fluctuations, we square both sides of Eq. (C14), take the expectation, and rewrite the temporal derivative in terms of the temporal power spectral density $F_a(\omega)$[15] as

$$\langle [R'(z, \Delta t)]^2 \rangle \approx \left[\frac{(\Delta t)^6}{32} \right]^2 \frac{1}{(\gamma - 1)^2} [1 - (z - z_0)\gamma H/\sigma_0^2]^2 \times \frac{1}{2\pi} \int_f^{\omega_c} \omega^{12} F_a(\omega) d\omega, \tag{C15}$$

where the lower limit of integration on the power spectral density corresponds to the inertial frequency f ($\sim$35 h), and the upper limit ω_c corresponds to the filter cutoff used during data processing, which takes on a maximum value of N, the buoyancy frequency. Using a model temporal power spectral density of the form[26]

$$F_a(\omega) = 2\pi \frac{f}{\omega^2} \langle r_a^2 \rangle, \tag{C16}$$

we find that the relative error in the ratio after averaging is

$$\left(\langle [R'(\Delta t)]^2\rangle\right)^{1/2} \approx \left(\langle r_a^2\rangle\right)^{1/2}\left(\frac{4}{11}\frac{f}{\omega_c}\right)^{1/2}\left[\frac{(\omega_c \Delta t)}{2}\right]^6 \times \frac{1}{(\gamma - 1)}\left[1 - (z - z_0)\gamma H/\sigma_0^2\right]. \tag{C17}$$

A comparison of Eq. (C17) with Eq. (C9) shows that the reduction in the density error for a temperature measurement that used the weighted-averaging procedure is

$$\left[\frac{2\pi \Delta t}{T_{\mathrm{rms}}}\right] \Bigg/ \left(\frac{4}{11}\frac{f}{\omega_c}\right)^{1/2}\left[\frac{(\omega_c \Delta t)}{2}\right]^6. \tag{C18}$$

If $\omega_c = N = 2\pi/5$ min (the buoyancy frequency) is used, then $f = 2\pi/35$ h (the inertial frequency), and the parameters from Table 6 are used, the reduction in the density error varies from ~75 for $\Delta t = 1$ min to >2000 for $\Delta t < 30$ sec. Similar expressions can be derived for wind measurements. The values calculated in Table 6 are scaled by the factor given in Eq. (C18) and listed in Table 3.

The authors wish to thank M. Gruebele for his time in discussing Na spectroscopy. This work has been partially supported by National Science Foundation grants ATM90–24367, DPP90–22467, and OPP92–19898DPP. D. Simonich was supported by grant 201686/92–9–NV from the Conselho Nacional de Desenvolvimento Científico e Technológicio (CNPq) of Brazil.

References

1. R. E. Bills, C. S. Gardner, and C. Y. She, "Narrowband lidar technique for sodium temperature and Doppler wind observations of the upper atmosphere," Opt. Eng. **30,** 13–21 (1991).
2. C. Y. She, J. R. Yu, J. W. Huang, C. Nagasawa, and C. S. Gardner, "Na temperature lidar measurements of gravity wave perturbations of winds, density, and temperature in the mesopause region," Geophys. Res. Lett. **18,** 1329–1331 (1991).
3. C. Y. She, J. R. Yu, and H. Chen, "Observed thermal structure of a midlatitude mesopause," Geophys. Res. Lett. **20,** 567–570 (1993).
4. R. E. Bills, C. S. Gardner, and S. J. Franke, "Na Doppler/temperature lidar: initial mesopause region observations and comparison with the Urbana medium frequency radar," J. Geophys. Res. **96,** 22701–22707 (1991).
5. C. S. Gardner, D. C. Senft, T. J. Beatty, R. E. Bills, and C. Hostetler, "Rayleigh and sodium lidar techniques for measuring middle atmosphere density, temperature and wind perturbations and their spectra," in *World Ionosphere/Thermosphere Study (WITS) Handbood*, C. H. Liu, ed. (Scientific Committee on Solar Terrestrial Physics, Urbana, Illinois, 1989).
6. J. M. C. Plane, "The chemistry of meteoric metals in the earth's atmosphere," Int. Rev. Phys. Chem. **10,** 55–106 (1991).
7. C. Y. She, J. R. Yu, H. Latifi, and R. E. Bills, "High-spectral-resolution fluorescence light detection and ranging for mesospheric sodium temperature measurements," Appl. Opt. **31,** 2095–2106 (1992).
8. K. H. Fricke and U. von Zahn, "Mesopause temperatures derived from probing the hyperfine structure of the D_2 resonance line of sodium by lidar," J. Atmos. Terr. Phys. **47,** 499–512 (1985).
9. R. M. Measures, *Laser Remote Sensing—Fundamentals and Applications* (Wiley, New York, 1984).
10. E. Arimondo, M. Inguscio, and P. Violino, "Experimental determinations of the hyperfine structure in the alkali atoms," Rev. Mod. Phys. **49,** 31–75 (1977).
11. I. M. Reid, "MF Doppler and spaced antenna radar measurements of upper middle atmosphere winds," J. Atmos. Terr. Phys. **50,** 117–134 (1988).
12. A. Corney, *Atomic and Laser Spectroscopy* (Oxford U. Press, Oxford, 1977).
13. B. Welsh and C. S. Gardner, "Nonlinear resonant absorption effects on the design of resonance fluorescence lidars and laser guide stars," Appl. Opt. **28,** 4141–4153 (1989).
14. P. von der Gathen, "Saturation effects in Na lidar temperature measurements," J. Geophys. Res. **96,** 3679–3690 (1991).
15. D. C. Senft and C. S. Gardner, "Seasonal variability of gravity wave activity and spectra in the mesopause region at Urbana," J. Geophys. Res. **96,** 17229–17264 (1991).
16. R. E. Bills and C. S. Gardner, "Iron and sodium Doppler/temperature lidar studies of the upper mesosphere," Rep. EOSL 91–002 (Electro-Optic Systems Laboratory, University of Illinois, Urbana, Ill., 1991).
17. A. Gaupp, P. Kuske, and H. J. Andrä, "Accurate lifetime measurements of the $^2P_{1/2}$ states in neutral lithium and sodium," Phys. Rev. A **26,** 3351–3359 (1982).
18. P. W. Atkins, *Molecular Quantum Mechanics* (Oxford U. Press, New York, 1983).
19. A. E. Siegman, *Lasers* (University Science, Mill Valley, Calif., 1986).
20. M. I. D'Yakonov, "Theory of resonance scattering of light by a gas in the presence of a magnetic field," Sov. Phys. JETP **20,** 1484–1489 (1965).
21. R. N. Zare, *Angular Momentum—Understanding Spatial Aspects in Chemistry and Physics* (Wiley, New York, 1988).
22. D. Zimmermann, "Determination of the lifetime of the $^4P_{1/2}$ state of potassium by Hanle-effect," Z. Phys. A **275,** 5–10 (1975).
23. International Association of Geomagnetism and Aeronomy, Division 1, Working Group 1, "International Geomagnetic Reference Fields: DGRF 1965, DGRF 1970, DGRF 1975 and IGRF 1980," EOS Trans. AGU **62,** 1169 (1981).
24. J. R. Morris, "Efficient excitation of a mesospheric sodium laser guide star by intermediate-duration pulses," J. Opt. Soc. Am. A **11,** 832–845 (1994).
25. P. W. Milonni and L. E. Throde, "Theory of mesospheric sodium fluorescence excited by pulse trains," Appl. Opt. **31,** 785–799 (1992).
26. C. A. Hostetler and C. S. Gardner, "Observations of horizontal and vertical wave-number spectra of gravity wave motions in the stratosphere and mesosphere over the mid-Pacific," J. Geophys. Res. **99,** 1283–1302 (1994).